The Effect of Surface Ligands on the Surface Chemical States and Photoluminescence Characteristics in Cesium Lead Bromide Perovskite Nanocrystals

Muhammad Asharuddin[a], Rahmat Hidayat[a*], Adhita Asma Nurunnizar[b], Natalita Maulani Nursam[b], Valdi Rizki Yandri[c], Waode Sukmawati Arsyad[d], Joko Suwardy[e], Efi Dwi Indari[e], and Yoshiyuki Yamashita[f,g*]

[a] Physics of Magnetism and Photonics Research Division, Faculty of Mathematics and Natural Sciences, Bandung Institute of Technology, Jl. Ganesha 10, Bandung 40132, West Java, Indonesia
[b] Research Center of Electronics, National Research and Innovation Agency, Jl. Sangkuriang, Bandung 40132, West Java, Indonesia
[c] Department of Electrical Engineering, Polytechnic State of Padang, Limau Manis Padang 25164, West Sumatra, Indonesia
[d] Physics Department, Faculty of Mathematics and Natural Sciences, Halu Oleo University, Anduonohu, Kendari, South East Sulawesi, 93232, Indonesia
[e] Research Center for Quantum Physics, National Research and Innovation Agency (BRIN), KST BJ Habibie Serpong, Banten, Indonesia 15314
[f] Nano Electronics Device Materials Group, Research Center for Electronic and Optical Materials, National Institute of Materials Science, 305-0044 1-1 Namiki Tsukuba Ibaraki, Japan
[g] Graduate School of Engineering, Kyushu University, Motooka 744, Nishi-ku, Fukuoka 819-0395, Japan

*corresponding authors: rahmat@itb.ac.id, yamashita.yoshiyuki@nims.go.jp

Abstract. This paper presents the results of our study on the relationship between the surface chemical states, which are influenced by ligands, and photoluminescence (PL) characteristics in cesium lead halide perovskite nanocrystals (NCs). NCs were synthesized via the Ligand-Assisted Reprecipitation (LARP) and Ultrasonic-Assisted (URSOA) methods, which were able to produce NCs with and without ligands. Although both synthesis methods used similar precursor composition and processing steps, the resulting crystal structures of NCs are different. The LARP method yielded orthorhombic $CsPbBr_3$ NCs, while the URSOA method yielded a mixture of hexagonal Cs_4PbBr_6 and orthorhombic $CsPbBr_3$ NCs with an approximate weight ratio of ~10:1. The X-ray diffraction data indicated that both NCs with and without ligands have the same crystal structure. However, as revealed from photoelectron spectroscopy analysis for NCs without ligands, the measured chemical states were found to be different between the inner side and the surface of NCs, which could be associated with surface defect species from the accumulation of Cs^+ atoms, Pb atoms with zero oxidation state, unbonded Br atoms, and Br vacancies near and at the surface of the NCs. The difference appears to be correlated with the observed photoluminescence (PL) characteristics. Although the photoelectron spectroscopies measured only the core level orbitals, the variation in the measured chemical states may correlate with electronic structure alteration in valence orbitals, which are involved in the photoexcitation and exciton relaxation mechanism. The PL of LARP NCs (orthorhombic $CsPbBr_3$) shows two components of PL decay, which are largely suppressed in NCs with purification or NCs without ligands. However, for URSOA NCs (predominantly Cs_4PbBr_6 NCs), the PL decays are almost similar for both with and without ligands. The present experimental data clearly show that the variations in photoluminescence (PL) characteristics, in addition to the crystal structure that determines the basic characteristics of the formed excitons, may also originate from the influence of surface states or surface defect species that are affected by surface ligands. This insight may be useful not only for the further development of passivation molecules in a general context but also for the design of buffer layer molecules in perovskite heterojunction devices.

Keywords. $CsPbBr_3$, Cs_4PbBr_6, halide perovskite nanocrystals, surface ligand, chemical states, photoluminescence

1. Introduction

Lead-halide perovskite nanocrystals (NCs) constitute a class of emerging materials of significant interest because of the possibility of tailoring their electronic and optical properties, which results in modifications of their bandgap energy, emission wavelength, and charge-carrier mobility. [1,2,3,4] Therefore, lead halide perovskite NCs have been much explored as promising nanomaterials for application in optoelectronic devices such as solar cells[5], photodetectors[6], lasers[7], and light-emitting devices.[8] Lead-halide perovskite materials can typically be classified into two categories based on the type of their cations, i.e., organic lead halide perovskites (often also referred as hybrid lead halide perovskites) and all inorganic lead halide perovskites. Organic lead halide perovskites incorporate organic monocation, such as methylammonium ($MA^+/CH_3NH_3^+$), formamidinium ($FA^+/CH_5N_2^+$), or other similar molecules.[9] Other halide anions, particularly Bromide (Br^-), have also been widely reported, which showed a larger open circuit voltage and better chemical stability despite a smaller power conversion efficiency compared to those with Iodide (I^-).[10] In contrast, instead of incorporating organic molecular cations, inorganic lead halide perovskites contain inorganic cations of alkali metals, the first group of the periodic table, such as rubidium (Rb)[11] and cesium (Cs). [12] Compared to organic lead halide perovskites, inorganic cesium lead halides exhibit better long-term stability under ambient conditions.[13]

Lead-halide perovskite NCs are usually synthesized by wet chemical processes, where various shapes of NCs can be obtained such as quantum dots (QDs), nanoplates, and nanowires .[14] Various methods, such as hot injection[15], solvent-induced reprecipitation[16], microwave-assisted (MA)[17], ultrasonic-assisted (URSOA)[18], and ligand-assisted reprecipitation (LARP) methods, have been developed to synthesize these perovskite NCs with relatively high products reproducibility and homogeneity.[19,20] The LARP method is the most widely utilized method because of high reproducibility with the possibility of varying ligands, precursors and solvents.[21] The ligands play important roles in dissolving the precursors, crystal seed formation, controlling crystal growth, and crystal surface encapsulation by the ligands.[22,23] In LARP, however, the crystal seed formation must be initiated by the addition of an antisolvent to the precursor solution.[24] Lead-halide perovskite QDs with high photoluminescence quantum yields are mostly synthesized using this LARP method.[25] In addition, by choosing appropriate ligands and their composition ratios, the synthesis can form NCs with a particular crystal structure, such as monoclinic, orthorhombic[26], tetragonal[27] or cubic structures.[27] Another synthesis method is the URSOA method, which also use a similar precursors and ligands as used in the LARP method. However, the URSOA method employ ultrasonic wave, which play important roles to initiate the nucleation of crystal seed and control the crystal growth.[18,28,29] This method does not require the heating of precursors and could be implemented as a "one pot" synthesis process. Molecular vibrations produced by ultrasonic waves cause local heating inside the precursor solution, allowing a rapid formation of NCs in an entirely room temperature environment.

The PL characteristics and stability of these lead halide perovskites have recently become a major focus of research. The PL properties of perovskite NCs have been assigned to be originated from excitons with various characteristics, such as free-excitons, self-trapped excitons (STEs), and exciton polarons.[30–32] The PL characteristics are also determined by crystal structure. $CsPbBr_3$, one of the most investigated lead halide perovskites, shows different PL wavelength and intensity depending on the crystal structure, namely orthorhombic[26], tetragonal[27], or cubic structures.[27] Various synthesis parameters, such as precursor concentrations, ligands, antisolvent polarity, etc., might significantly affect the PL characteristics of the synthesis products despite the products showing the same crystal structure.[30] Moreover, although the synthesized lead halide QDs or NCs show a perfect crystal structure, from the X-ray diffraction (XRD) measurement for instance, and can effectively absorb photons, some samples may show weak PL, suggesting the occurrence of strong non-radiative recombination pathways.[33,34] This non-radiative sites perhaps not present inside the NCs, but on the NCs surface.[35,36.] It is therefore important to understand the relationship between the PL characteristics and the surface chemical states, which may be influenced by surface ligands, to verify the cause of the observation of PL characteristic variation. However, only a limited number of studies have been reported in detail on the effect of ligands on the PL characteristics, the crystal structures of the NCs, and the surface chemical states at the NC surface.[13,33] Here, we report our study on the effects of ligands on the crystal structures of the cesium lead bromide perovskite NCs, the chemical states at the surfaces, and the PL characteristics by performing several characterizations using X-ray diffraction (XRD), X-ray photoelectron spectroscopy (XPS), hard X-ray photoelectron spectroscopy (HAXPES), and Fourier transform infrared spectroscopy (FTIR). This work establishes a direct correlation between surface states and PL characteristics that has not been explicitly addressed in previous studies, marking a distinct advance beyond conventional ligand engineering or passivation strategies. Among the aforementioned synthesis methods, in this study, we chose the LARP and URSOA methods for synthesizing cesium lead bromides because both LARP and URSOA can use the same composition and concentrations of precursors and ligands. In addition, those methods can produce both NCs with and without ligands, which are useful for achieving the aim of the present study.[18,27,37]

2. Experimental Section

2.1. Materials

Cesium bromide (CsBr, > 99.99%) and lead bromide ($PbBr_2$, < 99,99%), purchased from Tokyo Chemical Industry Co., Ltd., were used as the perovskite precursors. Linoleic acid (LA) and Oleylamine (OlAm) (purchased from Tokyo Chemical Industry Co., Ltd.) were used as ligands. Dimethyl sulfoxide (DMSO) and dimethylformamide (DMF) were used as precursor solvents to synthesize cesium lead bromide NCs. Toluene was used as the antisolvent, and ethanol was used as the solvent for the purification process. Analytical-grade solvents (Merck/Sigma Aldrich) were used without further purification.

2.2. Synthesis of Perovskite NCs

LARP Method. Fig. 1 schematically shows the main steps of the LARP method. This method is different from the hot injection method because the reaction takes place at room temperature (~28°C). Therefore, the crystal growth is accelerated by the addition of anti-solvent at the end of the synthesis process. In the present study, only the LA ligand was used in the synthesis. OlAm ligand, which is commonly reported in the literature,[37,38] was not used because OlAm needs a high temperature to be completely removed form nanoparticle surfaces.[39] High temperature treatment above 100°C may change the crystal structure of the resulted cesium lead bromide perovskites.[40] For preparing the precursor solution, CsBr (0.5 mol) and $PbBr_2$ (0.5 mol) were separately dissolved in a DMF:DMSO (7:3 v/v) mixed solvent. Subsequently, the CsBr solution was added dropwise to the $PbBr_2$ solution while stirred until a 1:1 volume ratio was achieved. The solution was then continuously stirred for 30 min.

The LA ligand was then added to the precursor solution with the volume ratio of the LA ligand and the precursor solution of 1:2. The solution was stirred again for 15 min. Finally, toluene, as the antisolvent. was added dropwise to the precursor solution to initiate the formation of the cesium lead bromide NCs.[27,37] The precipitated powder was dried in a vacuum chamber at 100°C until the remaining solvent completely evaporated. The powder was then stored and labeled as an unpurified NCs, or in other words, NCs with ligands (LARP-WOL).

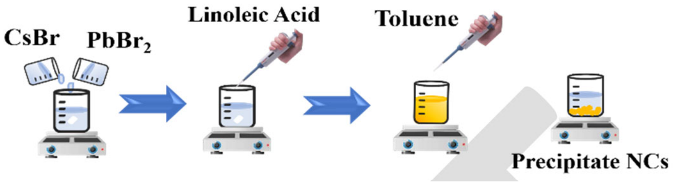

Fig. 1. Synthesis process of cesium lead bromide perovskite NCs via the rapid LARP method.

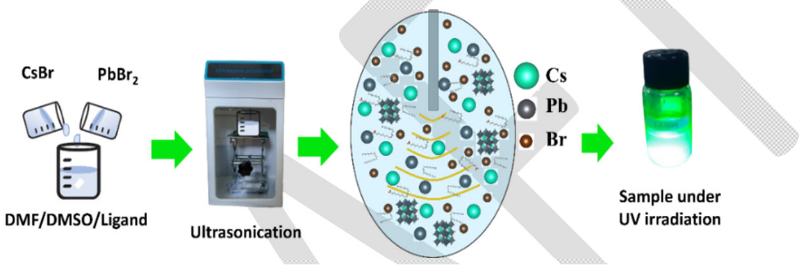

Fig. 2. The URSOA synthesis process of cesium lead bromide NCs.

To obtain cesium lead bromide NCs without ligands on their surface, the cesium lead bromide NC products were purified to remove the ligands by using a mixture solution of ethanol and toluene (1:1 v/v). The NCs product was added to the solution and then sonicated at 80 W for 10 min using an ultrasonic processor. A centrifuge was used to collect the cesium lead bromide NCs from the dispersion solution. Finally, these purified NCs were also dried in a vacuum chamber at 100°C to evaporate the remaining solvent. Herein, this purified NCs sample is referred to as NCs with purification (LARP-WOL). The average crystal sizes of these NCs without and with purification were estimated to be 29.64 nm for LARP-WL and 33.22 nm for LARP-WOL. These crystal sizes were estimated from the FWHMs of the XRD peak by using the Debye-Scherrer equation.[41]

URSOA Method. Fig. 2 schematically shows the main steps of the URSOA method. The URSOA method involves synthesis steps similar to those of the LARP method. However, in the URSOA method, instead of the use of anti-solvent, ultrasonication is used to initiate the seed formation of NCs. The synthesis process was initiated by mixing the precursors CsBr and $PbBr_2$ in the same molar ratio, followed by the addition of LA/OlAm ligands (LA:OlAm = 1:1) in a precursor-to-ligand ratio of 2:1 v/v. Subsequently, the solution mixture was ultrasonicated at 90 W for 10 min using an ultrasonic processor. Similarly to the final synthesis step of the LARP samples above, to obtain the NC products, the precipitate and solvent were separated using a centrifuge and vacuum dryer at 100°C. The products were referred to NCs with ligands (URSOA-WL). A similar synthesis process was also performed without ligands, where the products referred to as NCs without ligands (URSOA-WOL). The average crystallite sizes were estimated to be 34.64 nm for NCs with ligands (URSOA-WL) and 38.28 nm for NCs without ligands (URSOA-WOL). The names of the synthesized samples and the differences in their synthesis processes are summarized in Table 1.

Table 1. Sample names and their differences.

Sample name	Synthesis Method	LA ligand	OlAm ligand	Anti-solvent	Purification	Ultra-sonication	With ligands
LARP-WL	LARP	✓	×	toluene	×	×	✓
LARP-WOL	LARP	✓	×	toluene	✓	×	×
URSOA-WL	URSOA	✓	✓	×	×	✓	✓
URSOA-WOL	URSOA	×	×	×	×	✓	×

Note: × shows the treatment was not used, while ✓ shows it was used

2.3. Characterization methods

The XRD measurements were performed on dried powder for all samples of cesium lead bromide NCs using the SmartLab X-ray diffractometer (Rigaku, Japan). The wavelength was 1.5406 Å (Cu-Kα radiation). XPS and HAXPES measurements were performed using the Quantes (ULVAC-PHI). Al Kα (h*ν*:1486.6 eV) and Cr Kα (h*ν*:5414.8 eV) sources were used for XPS and HAXPES measurements, respectively. The total energy resolutions were 0.51 and 0.76 eV, respectively. The binding energies were calibrated using the binding energy of the C 1s core-level of the C-H bond of organic molecules (284.8 eV). To investigate the adsorbed states of the ligands of the NCs, Fourier Transform Infrared (FTIR) measurements (FTIR Alpha II, Bruker) were carried out utilizing the attenuated total reflection mode. The photoluminescence spectra of the cesium lead bromide NCs were measured using an Ocean Optics USB 2000 spectrometer with a 406 nm light source laser. The PL decays were measured using an experimental setup consisting of a pico-second laser (PicoQuant) at 420 nm (with 20 ps pulse width, 50 mW light power, and 10 MHz repetition rate), a photon microdevice detector, and a data acquisition interface (TimeHarp 260 from PicoQuant).[42]

3. Results and Discussion

3.1. Crystal structures, chemical states, and PL characteristics of Cesium Lead Bromide NCs prepared by LARP method

3.1.1. *Crystal structures and chemical states*

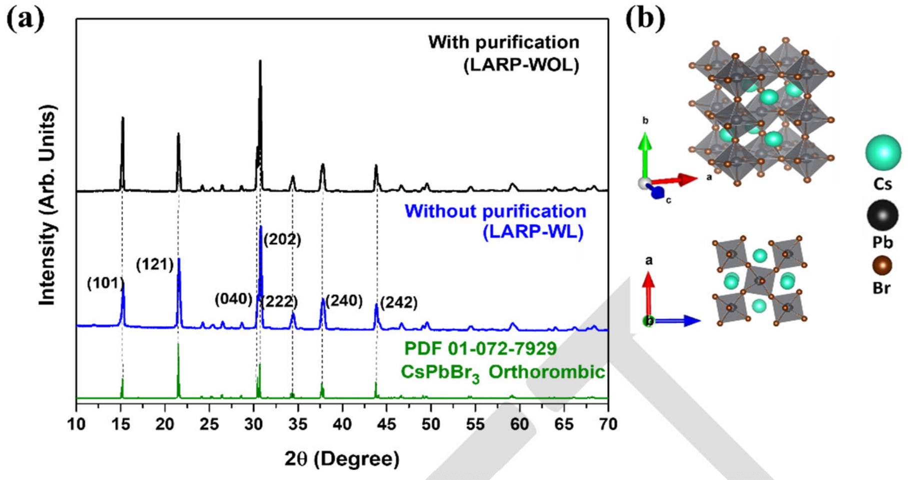

Fig. 3. (a) XRD patterns of the NCs with purification (LARP-WOL) and without purification (LARP-WL) and the reference data of the orthorhombic $CsPbBr_3$ (PDF-01-072-7929). (b) the top and the side views of crystal structure of orthorhombic $CsPbBr_3$.

The XRD measurements were performed to identify the crystal structures of the NCs prepared by the LARP method (LARP WOL and LARP-WL). The XRD patterns of both NCs, as shown in Fig. 3 (a), indicate the prominent peaks at 2θ = 15.2°, 21.6°, 30.5°, and 30.8°, which could be assigned to the (101), (121), (040), and (202) diffraction planes of orthorhombic $CsPbBr_3$ by referring the powder diffraction file PDF-01-072-7929 shown in Fig. 3Fig. 3 (a).[43] The crystal structure of the orthorhombic $CsPbBr_3$ is shown in Fig. 3 (b). The lattice constants were estimated to be a = 8.24 Å, b = 11.74 Å, and c = 8.2 Å. Because both NCs have the indistinguishable XRD patterns, the orthorhombic crystal structure remains unchanged after the purification process. However, in general, XRD shows the entire volume of the NCs, which is consequently insensitive to changes in the crystal surface.

Fig. 4 (a) and (b) show the Cs $3d_{5/2}$ core-level HAXPES spectra for the NCs without and with purification (LARP-WL and LARP-WOL), respectively. Both NCs exhibit one peak at 724.2 eV, which is attributed to the Cs atoms in the $CsPbBr_3$ NCs.[44,45] Fig. 4 (c) and (d) show the Pb 4f core-level HAXPES spectra for the NCs without and with purification (LARP-WL and LARP-WOL), respectively, which show two peaks at Pb $4f_{7/2}$ (138.2 eV) and Pb $4f_{5/2}$ (143.1 eV). These peaks are attributed to the Pb atoms in $CsPbBr_3$ NCs.[46] Fig. 4 (e) and (f) show the Br 3d core-level HAXPES spectra for the NCs without and with purification (LARP-WL and LARP-WOL). Both samples have one component (Br $3d_{5/2}$ (68.2 eV) and Br $3d_{3/2}$ (69.2 eV)), which is due to the Br atoms in $CsPbBr_3$ NCs.[27,47] Because HAXPES exhibits bulk chemical information (the information depth of ~10 nm[46]), the chemical states of the inner side of the NCs might not be affected by the surface ligands and the purification processes.

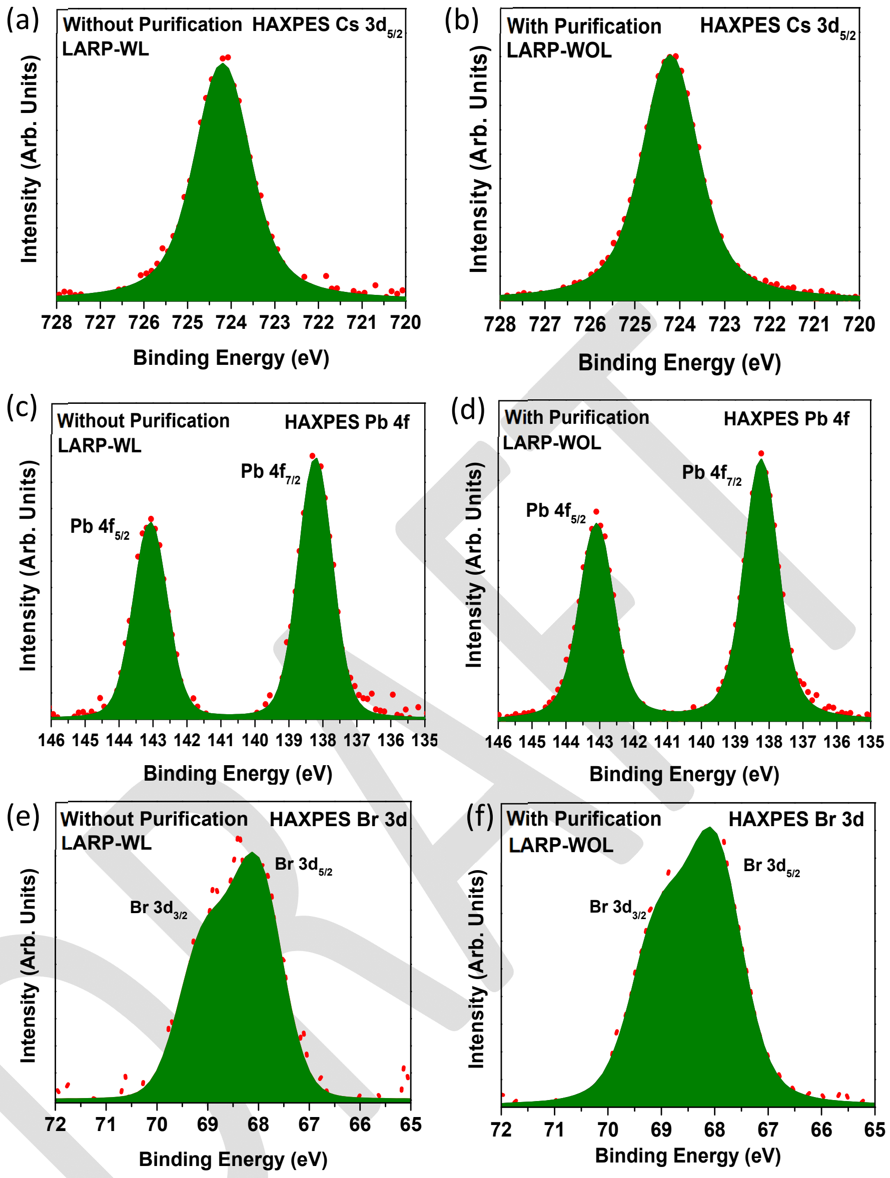

Fig. 4. HAXPES spectra of the NCs without (LARP-WL) and with purification (LARP-WOL) (a) and (b) for Cs $3d_{5/2}$; (c) and (d) for Pb 4f; and (e) and (f) for Br 3d, respectively.

XPS measurements were performed to investigate the surface chemical states of the NCs. Note that XPS exhibits relatively surface sensitive method in which the information depth is ~ 3 nm.[48,49] Fig. 5 (a) shows the survey XPS spectra of both NCs, showing the presence of Cs, Pb, Br, C, and O atoms in the $CsPbBr_3$ NCs. These NCs show significant differences between the peak intensities of the C 1s and O 1s core-levels, where the NCs without purification (LARP-WL) show higher peak intensities of C 1s and O 1s than the NCs with purification (LARP-WOL). Fig. 5 (b) shows the C 1s spectrum of the NCs without purification (LARP-WL), which can be deconvoluted into three components. The peak at 284.8 eV is attributed to C-C and C-H bonds of the LA molecules, whereas the peaks at 285.3 eV and 289.3 eV are associated with C=C and O-C=O bonds of the LA molecules, respectively.[50] For the O 1s spectrum (Fig. 5 (c)), there are two components observed at 532.4 eV and 533.7 eV, which are attributed to O-C and O-C=O bonds of the LA molecules, respectively.[50,51] Fig. 5 (d) and (e) show the C 1s and O 1s core-level XPS spectra for the NCs with purification (LARP-WOL), showing a drastic decrease in the areal peak intensities comparing to the case of the NCs without purification (LARP-WL). Therefore, the ligands at the $CsPbBr_3$ NC surface are removed by the purification process. The peaks at 284.4 eV and 532.3 eV for respective C 1s and O 1s core-levels may be attributed to the surface contaminations formed by sample preparation process[52], which are usually observed in XPS spectra.[53]

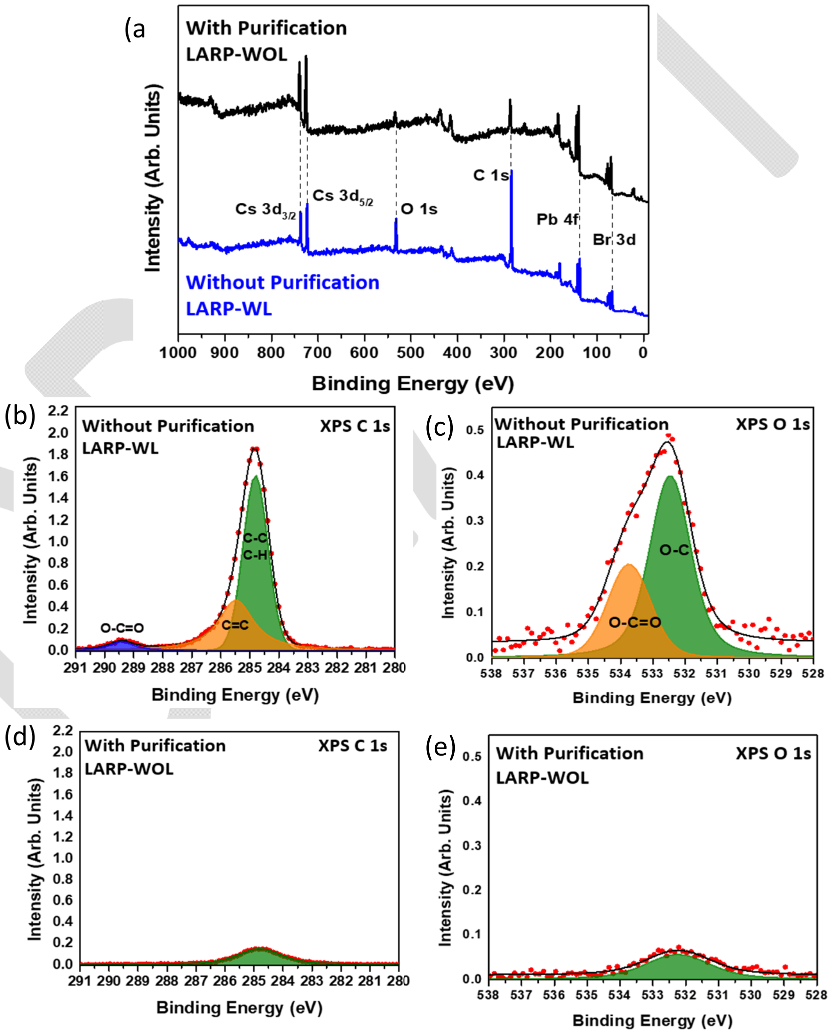

Fig. 5. XPS spectra survey for the NCs without (LARP-WL) and with purification (LARP-WOL) (b) C 1s and (c) O 1s of the NCs without purification (LARP-WL). (d) C 1s and (e) O 1s of the NCs

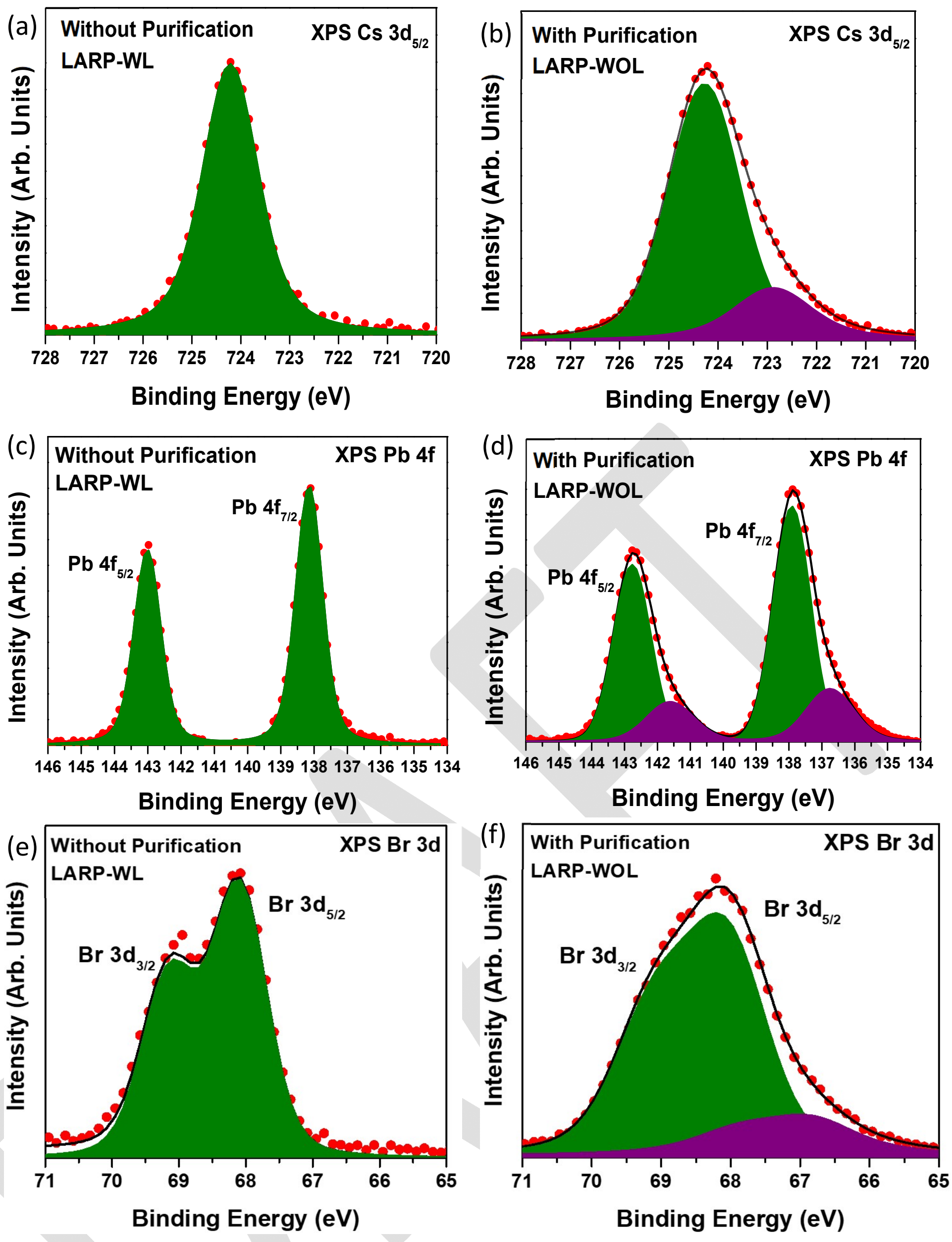

Fig. 6. XPS spectra of the NCs without (LARP-WL) and with purification (LARP-WOL); (a) and (b) for Cs $3d_{5/2}$; (c) and (d) for Pb 4f; and (e) and (f) for Br 3d, respectively.

Fig. 6 (a) shows the Cs $3d_{5/2}$ core-level XPS spectrum of the NCs without purification (LARP-WL). There is one peak at 724.2 eV, which is attributed to the Cs atoms in $CsPbBr_3$ NCs.[44,45] Fig. 6 (b) shows the Cs $3d_{5/2}$ core-level XPS spectrum of the NCs with purification (LARP-WOL). There are two components at 724.2 and 722.9 eV. The higher binding energy component at 724.2 eV (green component shown in Fig. 6 (b)) could be attributed to the Cs atom in $CsPbBr_3$ NCs[44,45], whereas the lower-binding-energy component at 722.9 eV (purple component) might be due to Cs^+ accumulation at the surface.[54,55] Fig. 6 (c) and (d) show the Pb 4f core-level spectra of the NCs without and with purification. The NC without purification (LARP-WL) (Fig. 6 (c)) has one component (Pb $4f_{7/2}$ (138.2 eV) and Pb $4f_{5/2}$ (143.1 eV)), which is attributed to the Pb atoms in $CsPbBr_3$ NCs.[46] In contrast, the NC with purification (LARP-WOL) (Fig. 6 (d)) has two components. The higher binding energy component (Pb $4f_{7/2}$ (138 eV) and Pb $4f_{5/2}$ (142.9 eV)) is attributed to the Pb atom in $CsPbBr_3$ NCs, whereas the lower binding energy state (Pb $4f_{7/2}$ (136.8 eV) and Pb $4f_{5/2}$ (141.7 eV)), might be due to Pb atom with oxidation state of zero (Pb^0) which might not bond with the Br atoms and could be present at the NCs surface.[55–57]

The Br 3d core-level XPS spectra for the NCs without and with purification (respective LARP-WL and LARP-WOL) are shown in Fig. 6 (e) and (f). For the NCs without purification (LARP-WL) (Fig. 6 (e)), the Br 3d core-level spectrum has one component (green color). The green component at 68.2 eV (Br $3d_{5/2}$) and 69.2 eV (Br $3d_{3/2}$) could be originated from the Br atoms in $CsPbBr_3$ NCs.[27,47] In contrast, for the NCs with purification (LARP-WOL) (Fig. 6 (f)), the Br 3d XPS spectrum shows two components. The component at 68.0 eV (Br $3d_{5/2}$) and 69.0 eV (Br $3d_{3/2}$) (green color) could be originating from the Br atom in the $CsPbBr_3$ NCs.[27,47] The lowest binding energy component at 66.8 eV (Br $3d_{5/2}$) and 67.8 eV (Br $3d_{3/2}$) (purple color) might be due to unbonded Br atoms present at the NC surface.[58] All core-level spectra were fitted using a Voigt profile function, and the detailed fitting parameters are provided in the Supplementary Information (Table S1 and S2).

In order to investigate the chemical species of the ligands before and after purification, the FTIR measurements were performed for those NCs prepared by LARP methods. Fig. 7 shows the FTIR spectra of the NCs without purification (LARP-WL) and with purification. (LARP-WOL). For the NCs without purification (LARP-WL), a strong vibration peak at 1712.9 cm^{-1} is attributed to the C=O (carbonyl) stretching vibration mode of the LA molecules whereas the peak at 2850–2924 cm^{-1} is due to symmetric and asymmetric vibrations of CH_2 groups.[38,59,60] The peak at 3012 cm^{-1} is originated from C-H stretching in the C=C-H species.[61] For the NCs with purification (LARP-WOL), although the intensities of those vibration bands are drastically decreased, several vibration bands such as C=O (at 1710.5 cm^{-1}) and C-H vibrations (at 2848.6 cm^{-1} and 2921.6 cm^{-1}) are still observed, indicating that an extremely small residue of the LA molecules remains after the purification. Further the details in the vibration band assignments of these FTIR spectra are shown in the Supplementary Information (Table S3). Note that these FTIR results are consistent with the C 1 s XPS results described above, where significantly weak components of C 1s and O 1s remain after purification process (LARP-WL) as shown in Fig. 5 (a).

From XRD, HAXPES, XPS, and FTIR results, the structural models before and after purification are proposed in Figs. 8Fig. 8 (a) and (b). Before purification (Fig. 8 (a)), the LA ligands are attached to the surface of the NCs. The carboxylate group of the ligands, which are negatively charged (COO^-)[62], might bond to the positively charged Pb^{2+} and Cs^{+} at the NC surface. As a result, the ligands could passivate the surface atoms, thus preventing the formation of defect species at the NC surface. After the purification process (Fig. 8 (b)), the ligands are removed leading to random the crystal periodicity termination at NC surface, forming the accumulation of Cs cations, Pb^0, and unbonded Br. In addition, the Br anions might be also detached from the NC surface after purification, resulting in the formation of Br vacancies. Our results suggest that the ligands might effectively prevent the formation of defect species at the NCs surface.

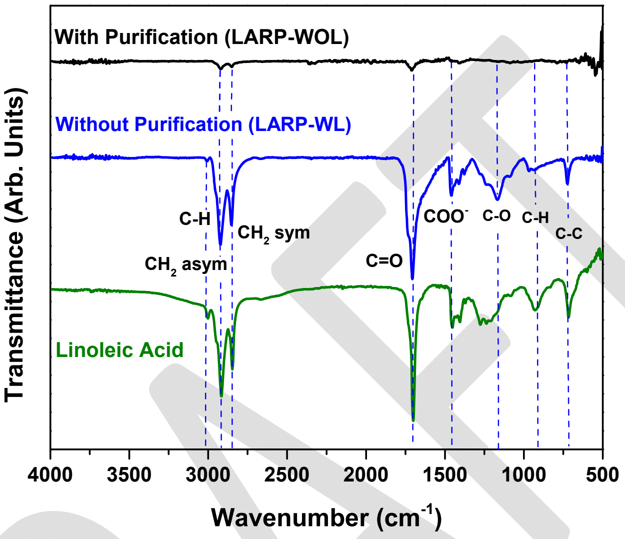

Fig. 7. FTIR spectra of the NCs without purification (LARP-WL) and with purification (LARP-WOL). The FTIR spectrum of the LA ligand is also shown as a reference in the vibration component assignments.

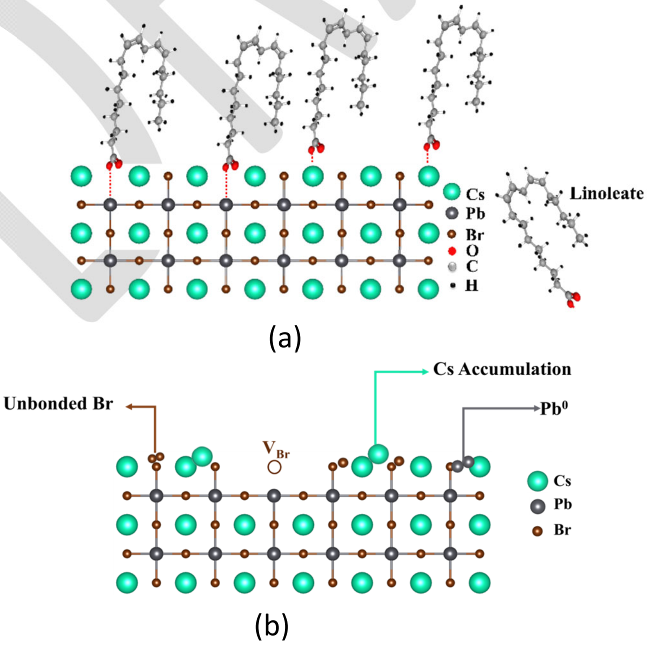

Fig. 8. Possible structures of the NCs near the surface (a) before and (b) after purification.

3.1.2. ***PL characteristics***

Fig. 9 (a) shows the PL spectra of the NCs without purification (LARP-WL) and with purification (LARP-WOL). The NCs without purification (LARP-WL) exhibit a shorter wavelength peak and higher PL intensity compared to the NCs with purification (LARP-WOL). Weak PL intensity observed at the NCs without purification (LARP-WL) might be attributed to the surface defect species[63,64], such as the accumulation of Cs^+, Pb^0, unbonded Br atoms, and Br vacancies at the NC surface. These defect species might form trap states in the bandgap and act as non-radiative recombination centers, decreasing the PL intensity.[65] For the observed red-shift peak, Liu *et al*. have conducted computational studies on the electronic structure of $CsPbBr_3$ NCs and have shown that $CsPbBr_3$ NCs with Br vacancies have a smaller band gap in comparison to the defect free $CsPbBr_3$ NCs.[66] Thus, the observed red-shift for the NCs with purification (LARP-WOL) may be thus caused by the Br vacancies formed at the NC surface.[67]

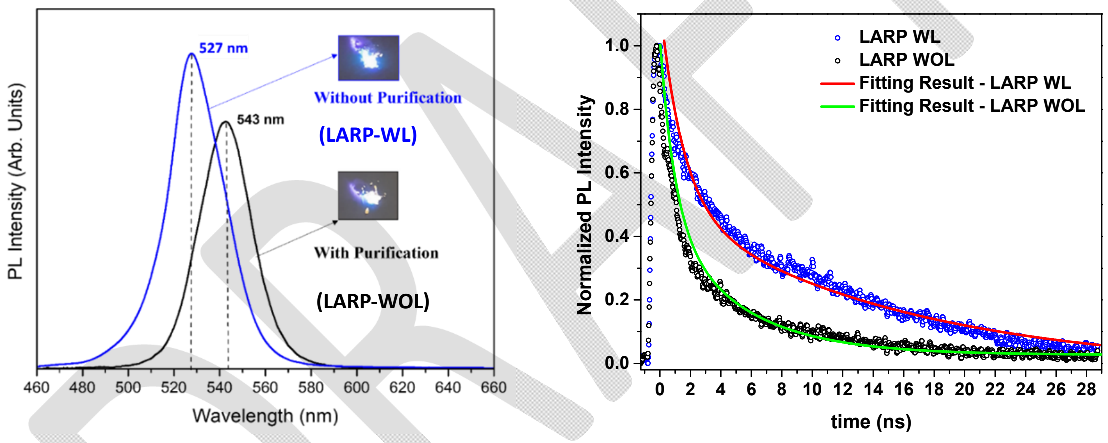

(a) (b)

Fig. 9. (a) PL spectra of the NCs without (LARP-WL) and with purification (LARP-WOL). (b) The normalized intensity of PL as a function of time measured for the LARP-WL and LARP-WOL NCs. The fitting results are shown as solid lines.

Fig. 9(b) shows the PL intensity as a function of time (decay) for NCs with and without purification, indicating that the PL decay of the NCs with purification (LARP-WOL) exhibits more rapid decay compared to the case of the NCs without purification (LARP-WL). According to the previous studies, the PL intensity as a function of time (decay) can be fitted with a bi-exponential function consisting of the fast and the slow decay components, which is given by[68,69]

$$I(t) = I_1 \exp\left(\frac{-t}{\tau_1}\right) + I_2 \exp\left(\frac{-t}{\tau_2}\right), \quad (1)$$

where I(t) represents the PL intensity at the time t, I_1 and I_2 denote the initial intensities of the fast and the slow decay components, and τ_1 andτ_2 denote the decay time constants of the fast and the slow decays, respectively. The average decay time (τ_{avg}) can be calculated using the following equation[69] :

$$\tau_{avg} = \frac{I_1{\tau_1}^2 + I_2{\tau_2}^2}{I_1\tau_1 + I_2\tau_2} \quad (2)$$

The decay parameters obtained from fitting results are shown in Table 2. The fast decay component could be ascribed to the radiative recombination of free excitons, whereas the slow decay could be associated with the radiative recombination of trapped excitons.[70,71] Longer decay time for the NCs without purification (LARP-WL) might indicate that the radiative recombination of free excitons could be dominant.[72] In contrast, faster decays in the NCs with purification (LARP-WOL) may be explained by non-radiative recombination via defect states.[69,73]

According to the previous report, the fast decay is originated from the free exciton recombination, and the recombination occurs at the inner side of NCs[70]. On the other hand, the slow decay due to the trapped exciton may occur mainly at the NC surface.[71] In the case of the NCs with purification (LARP-WOL), the surface defect species such as accumulation of Cs, Pb^0, the unbonded Br atoms, and the Br vacancies could trap the excitons as non-radiative centers, resulting in shorter lifetime for radiative recombination and dominance of non-radiative recombination. A similar trend was observed in the average decay time, where NCs without purification (LARP-WL) is longer than NCs with purification (LARP-WOL), indicating that ligands effectively suppress non-radiative recombination pathways and prolong carrier lifetimes.

Table 2. The fitting results obtained from curve fittings of PL decays in Fig. 9 using a bi-exponential decay function. I_1 and I_2 are the normalized initial intensities.

Sample	I_1	**τ_1 (ns)**	I_2	**τ_2 (ns)**	**τ_{avg} (ns)**
NCs without purification (LARP-WL)	0.58	1.77	0.50	14.12	12.55
NCs with purification (LARP-WOL)	0.56	0.98	0.43	5.02	4.20

3.2. Crystal structures, chemical states and PL characteristics of Cesium Lead Bromide NCs prepared by URSOA

3.2.1. *Crystal structures and chemical states in the NCs*

The XRD patterns of the NCs without and with ligands prepared by the URSOA method (URSOA-WOL and URSOA-WL) are shown in Fig. 10 (a). These NCs show not only the indistinguishable XRD patterns of the NCs prepared by the LARP method but also exhibit additional XRD peaks observed only by the URSOA method. By comparison with the reference XRD data PDF- 01-077-8224, the diffraction peaks at 12.7°, 12.9°, 20.1°, 22.5°, 25.5°, 27.7°, 28.6°, 30.3°, 30.9°, 34.2° and 38.9° could be assigned to the crystal planes (012), (110), (113), (300), (024), (131), (214), (223), (006), (134), and (324) of Cs_4PbBr_6 with hexagonal crystal structure.[18,69] The lattice constant was estimated to be a=b=13.72 Å and c=17.32 Å, with $\alpha=\beta=90°$ and $\gamma=120°$.[74,75] In addition, in comparison with PDF-01-072-7929, the peaks at 29°, 30.7°, 34.6°, and 43.7° can be assigned to the (122), (202), (103), and (242) planes of the orthorhombic $CsPbBr_3$ crystal structure.[27,69] The lattice constant was estimated to be a = 8.24 Å, b = 11.74 Å, and c = 8.2 Å. These XRD patterns indicate the formation of both $CsPbBr_3$ and Cs_4PbBr_6 crystal phases in the NCs prepared by URSOA method.

It should be noted that $CsPbBr_3$ exhibits a three-dimensional (3D) perovskite structure with orthorhombic structure (*Pnma* space group) at room temperature. This phase compose of a continuous network of corner-sharing $[PbBr_6]^{4-}$ octahedra, where Cs^+ ions occupy the interstitial A-site positions within the perovskite framework[76], as shown in Fig. 10 (b). In contrast, Cs_4PbBr_6 has a hexagonal crystal structure (*R-3 c* space group)[18,77], like an array or cluster of isolated $[PbBr_6]^{4-}$ octahedra groups connected with Cs^+ ions, which act as spacers to maintain the separation between octahedra, as shown in Fig. 10 (c).[18] Therefore, regardless of the presence of the ligands, two distinct phases of the perovskite crystals are formed, namely orthorhombic $CsPbBr_3$ and hexagonal Cs_4PbBr_6 crystal structures. By performing quantitative phase-analysis using the Rietveld method, the XRD patterns can be analyzed to determine the proportion of each phase.[78] The phase molar ratios of Cs_4PbBr_6 to $CsPbBr_3$ for the NCs with and without ligands (respective URSOA-WL and URSOA-WOL) were estimated to be 10.1:1 and 11.5:1, respectively, which are relative good agreement with the other studies.[69,79,80]

Fig. 11 (a) and (b) show the Cs $3d_{5/2}$ core-level HAXPES spectra for the NCs with and without ligands (URSOA-WL and URSOA-WOL). These HAXPES spectra were fitted by referring to the phase molar ratios of Cs_4PbBr_6:$CsPbBr_3$, based on the XRD analysis results above, at 10.1:1 for URSOA-WOL and 11.5:1 for URSOA-WL. The component at 724 eV (green color peak) can be assign to the Cs atoms in the $CsPbBr_3$ NCs, whereas the lower binding energy component at 723.3 eV (cream color peak) can be assigned to the Cs atoms in the Cs_4PbBr_6 NCs.[44,45,81] Fig. 11 (c) and (d) show the Pb 4f core-level HAXPES spectra for the NCs with and without ligands (URSOA-WL and URSOA-WOL), which also indicate that the Pb atoms exhibit two different chemical states. The lower binding energy component at 137.4 eV (Pb $4f_{7/2}$) and 142.3 eV (Pb $4f_{5/2}$)) is attributed to the Pb atoms in the Cs_4PbBr_6 NCs [82], whereas the higher binding energy component at 138.0 eV (Pb $4f_{7/2}$) and 142.8 eV (Pb $4f_{5/2}$) could be due to the Pb atom in the $CsPbBr_3$ NCs.[46] Fig. 11 (e) and (f) show the Br 3d core-level HAXPES spectra. The component at 67.2 eV (Br $3d_{5/2}$) and 68.2 eV (Br $3d_{3/2}$) could be attributed to the Br atoms of the Cs_4PbBr_6 NCs [28,83], whereas the higher binding energy component (green color) peaked at 68.2 eV (Br $3d_{5/2}$) and 69.2 eV (Br $3d_{3/2}$) could be due to the Br atoms of the $CsPbBr_3$ NCs.[28] Therefore, the chemical states of the inner side of the NCs are not affected by the presence and absence of the ligands.

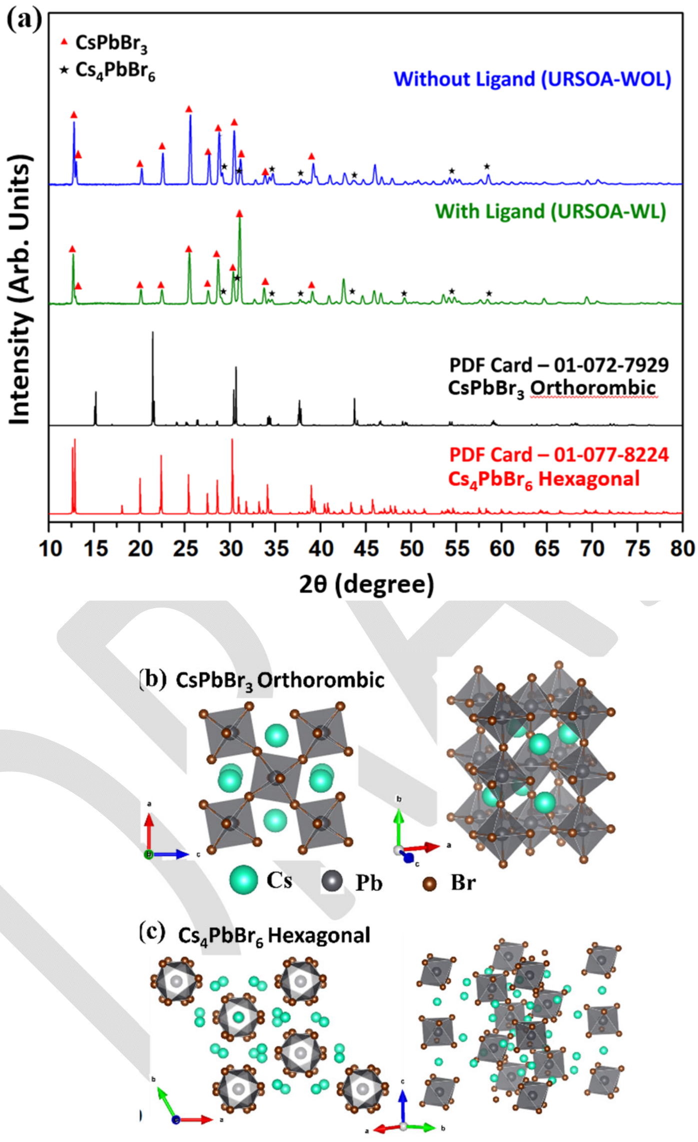

Fig. 10. XRD patterns of the NCs without (blue line) and with (green line) ligands. The (★) symbol indicates the diffraction peak from $CsPbBr_3$ phase, whereas the (▲) symbol indicates the diffraction peak from Cs_4PbBr_6 phase. Reference data for orthorhombic $CsPbBr_3$ (PDF-01-072-7929) (black line) and hexagonal Cs_4PbBr_6 (PDF-01-077-8224) (red line) are also shown for comparison. (b) The orthorhombic crystal structure of $CsPbBr_3$ (*Pnma* space group) and (c) the hexagonal crystal structure of Cs_4PbBr_6 (*R-3 c*

Fig. 12 (a) shows the survey XPS spectrum of the NCs with and without ligands (URSOA-WL and URSOA-WOL), showing a substantial difference in the peak intensities of C 1s and O 1s; the NCs with ligands (URSOA-WL) have much higher peak intensities of C 1s and O 1s than the NCs without ligands (URSOA-WOL). Fig. 12 (b) shows the C 1s spectrum of the NCs with ligands (URSOA-WL), which can be deconvoluted into three components. The peak at 284.8 eV is attributed to the C atoms of C-C and C-H bonds of the LA and the OlAm molecules, whereas the peaks at 285.4 eV and 288.1 eV are due to the C atoms of C=C/C-N and O-C=O bonds of the LA and the OlAm molecules, respectively.[50] For the O 1s XPS spectrum of the NCs with ligands (URSOA-WL) (Fig. 12 (c)), there are two components at 532.2 eV and 533.6 eV, which might be attributed to O-C and O-C=O bonds of the LA and the OlAm molecules, respectively.[50,51] The weak peak intensities of the C 1s and O1s core-levels of the NCs without ligands (URSOA-WOL), as shown in Fig. 12 (d) and (e), might be originated from the contaminants formed by sample preparation process.[52]

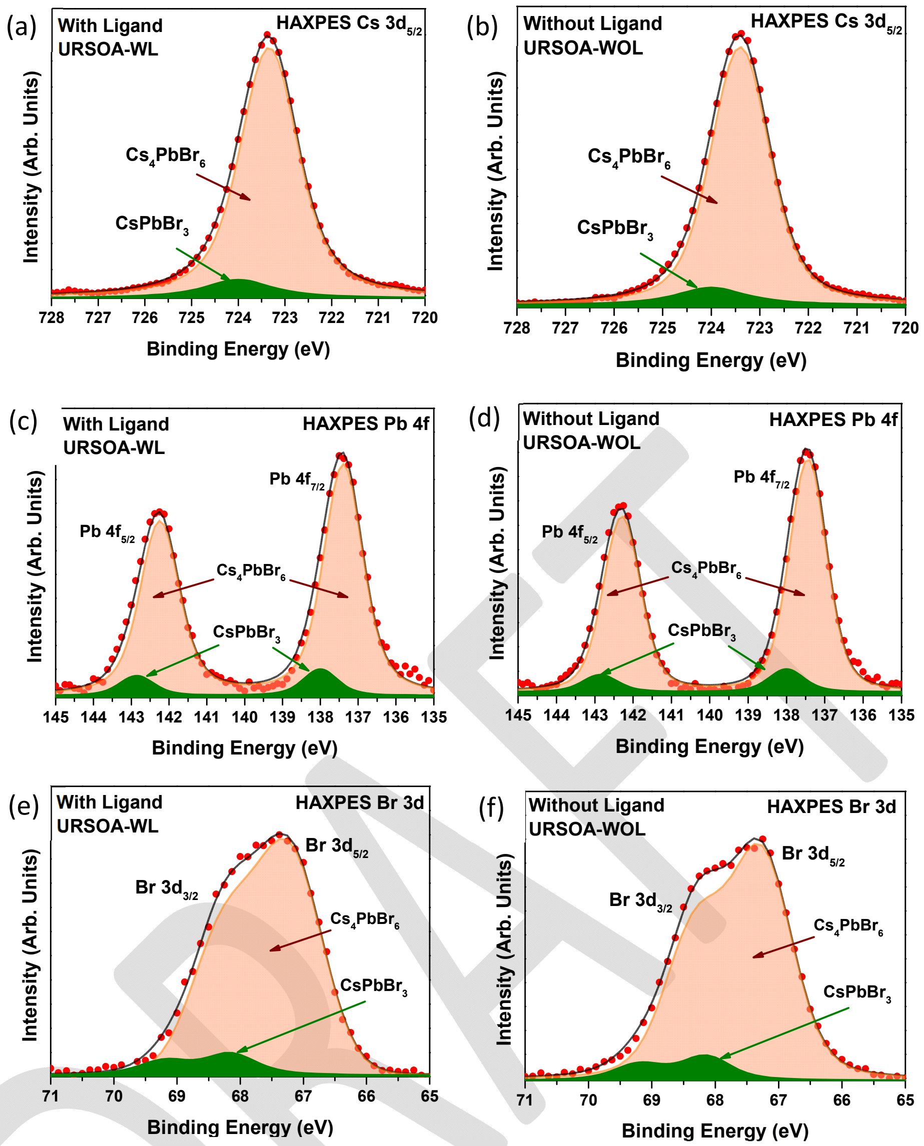

Fig. 11. HAXPES spectra for the NCs with (URSOA-WL) and without ligand (URSOA-WL): (a) and (b) for Cs 3d;$_{5/2}$ (c) and (d) for Pb 4f; and (e) and (f) for Br 3d, respectively.

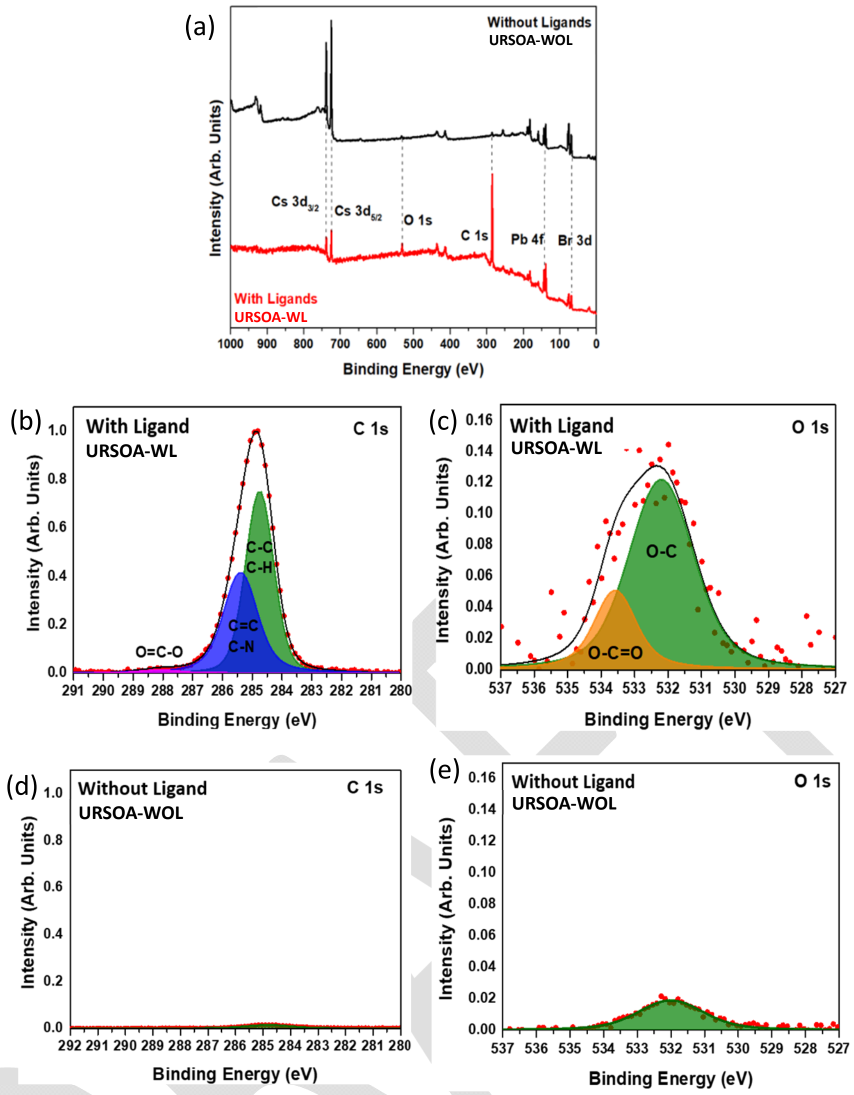

Fig. 12. (a) XPS survey spectra for the NCs with and without ligands. XPS spectra for (b) C 1s and (c) O 1s of NCs with ligands (URSOA-WL). XPS spectra for (d) C 1s and (e) O 1s of NCs without ligands

Fig. 13 (a) shows the Cs 3d$_{5/2}$ core-level XPS spectrum for the NCs with the ligands (URSOA-WL). The higher binding energy component at 724 eV is attributed to the Cs atom in the $CsPbBr_3$ NCs (green color)[45], whereas the lower binding energy component at 723.3 eV is due to the Cs atom in Cs_4PbBr_6 NCs (cream color).[28] In contrast, for the NCs without ligands (URSOA-WOL), there are three components as shown in Fig. 13 (b). The highest and the second highest binding energy components at 724 eV and 723.3 eV are attributed to the Cs atom in the $CsPbBr_3$ and the Cs_4PbBr_6 NCs, respectively.[28,45] The lowest binding energy component at 722 eV (purple color) might be attributed to the accumulation of Cs^+ at the surface of the NCs.[54,55]

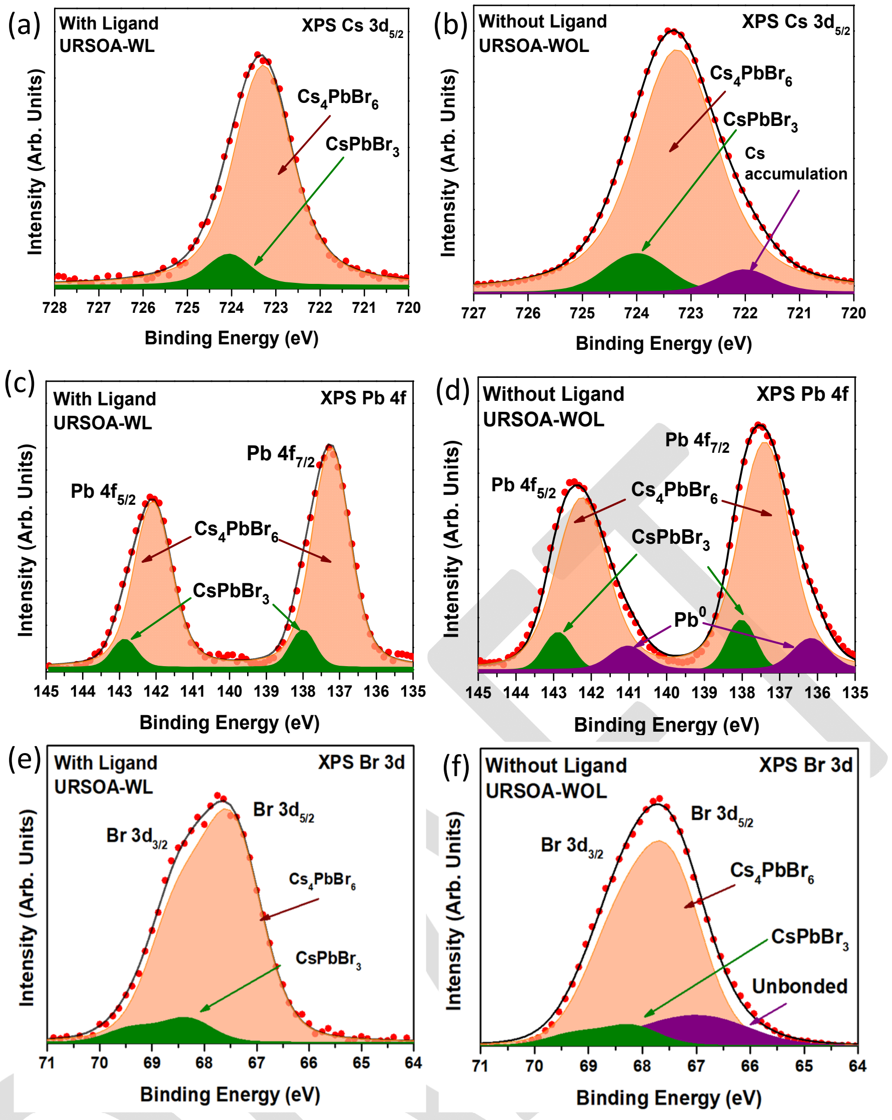

Fig. 13. XPS spectra of the NCs with (URSOA-WL) and without ligands (URSOA-WOL); (a) and (b) Cs 3d$_{5/2}$; (c) and (d) Pb 4f; and (e) and (f) Br 3d, respectively.

Fig. 13 (c) and (d) show the Pb 4f XPS spectra for the NCs with and without ligands (URSOA-WL and URSOA-WOL). For the NCs with the ligands (URSOA-WL), the highest and the second highest binding energy peaks at 138.0 eV and 137.3 eV could be attributed to the Pb atoms in the CsPbBr$_3$ and Cs$_4$PbBr$_6$ NCs, respectively.[82] In contrast, for the NCs without the ligands (URSOA-WOL), the components at the highest binding energy and the second highest binding energy can be attributed to the Pb atoms in the CsPbBr$_3$ and the Cs$_4$PbBr$_6$ NCs, respectively. The lowest binding energy component observed at 136.2 eV (purple color) might be attributed to Pb^0.[46,57] Fig. 13 (e) shows the Br 3d spectrum of the NCs with ligands (URSOA-WL). The green color components are attributed to the Br atoms in CsPbBr$_3$ NCs,[27,47,84] whereas the cream color components might be due to the Br atoms in Cs$_4$PbBr$_6$ NCs.[28,84] On the other hand, for Br 3d spectrum of the NCs without ligands (URSOA-WOL), there is one additional component (purple color) observed at 66.7 eV (Br $3d_{5/2}$) (Fig. 13 (f)), which may be attributed to the unbonded Br atoms present at the NCs surface.[58]

Fig. 14 shows the FTIR spectra of the NCs with and without ligands (URSOA-WL and URSOA-WOL). The NCs with ligands (URSOA-WL) show similar vibrational peaks to the LA (green) and the OlAm (magenta) molecules, indicating that the LA and the OlAm molecules could bond to the NC surface. The bands at 2919 and 2849 cm^{-1} correspond to asymmetric and symmetric stretching vibration mode of the $–CH_2–$ groups[38,59,60] in long-chain alkyl groups of both LA and OlAm molecules. A weak shoulder around 3006 cm^{-1} corresponds to C-H stretching mode.[59] The vibration peak at 1731 cm^{-1} is attributed to the C=O (carbonyl) stretching vibration mode of the LA molecules. The absorption at 1538 cm^{-1} is attributed to the asymmetric stretching vibration mode of COO^- of the carboxylate group, whereas the band around ~1400 cm^{-1} corresponds to symmetric stretch mode of COO^- of the carboxylate group, indicating the deprotonated carboxylic acid of the LA molecules. Additionally, a band around 1500 cm^{-1} is assigned to N–H bending mode[38,85], which is due to amine species of the OlAm molecule.[60] The peak at 1019 cm^{-1} is assigned to the C–N stretching vibration modes of the OlAm molecule.[86] In contrast, for the NCs without ligand (URSOA-WOL), the vibrational peaks corresponding to the LA and the OlAm molecules are hardly ever observed, indicating the LA and the OlAm molecules could not bond to the NC surface. The detail vibrational band assignments for the FTIR spectra of these samples are provided in the Supplementary Information (Table S4).

Fig. 15 (a) shows the proposed surface structure of the NCs with ligands obtained from XRD, HAXPES, XPS, and FTIR results. In the case of URSOA-WL, the LA and the OlAm molecules could interact with the NC surface. The carboxylate groups of the LA molecules may form a bonding with the Cs and the Pb cations at the outermost crystal sites, or they may also attach at the Br vacancies on the NC surface.[62] In the case of the OlAm molecules, the amine group ($−NH_2$) might be positively charged due to the formation of $-NH_3^+$[87,88], which might bond to the Br anions at the NC surface. The amine group enables the OlAm ligand to bond specifically to Br anion at the outermost NCs surface. Thus, these ligands are able to passivate the surface defects and inhibit the presence of uncoordinated atoms. On the other hand, the NCs without ligand (URSOA-WOL) exhibit the formation of surface defect species such as the accumulation of Cs^+, Pb^0, unbonded Br atoms, and Br vacancies at the NC surface. Therefore, the ligands effectively prevent the formation of defects near the surface of the NCs.

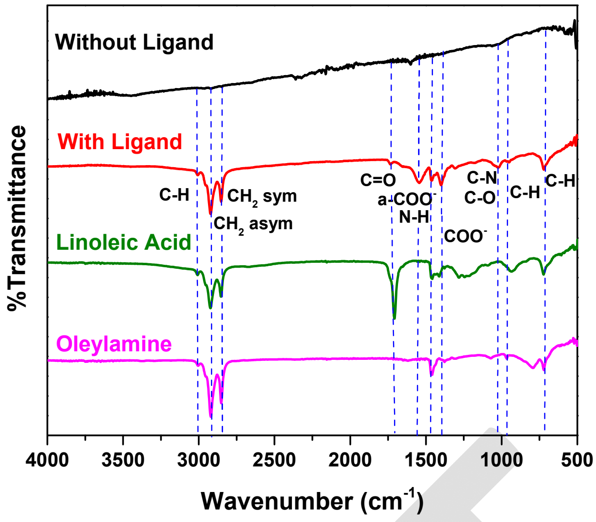

Fig. 14. FTIR spectra of the NCs without ligands (URSOA-WOL) and with ligands (URSOA-WL). The FTIR spectra of LA and OlAm ligands are also shown as the references.

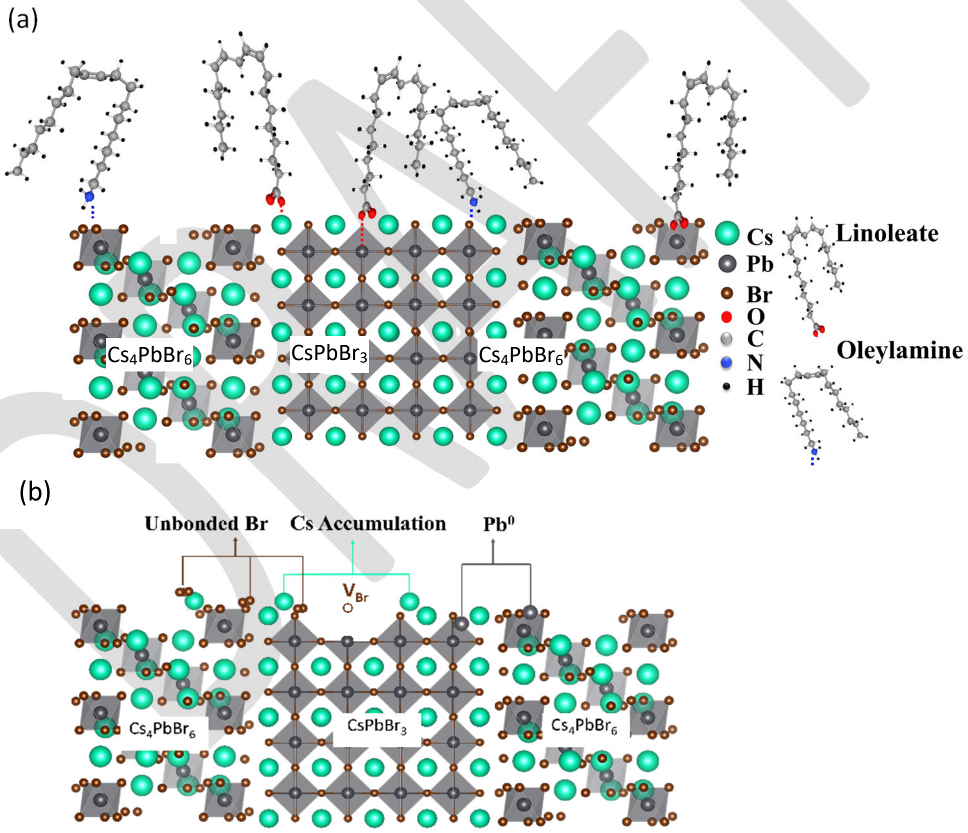

Fig. 15. Structural models of the NC near the surface (a) with ligands (URSOA-WL) and (b) without ligands (URSOA-WOL).

3.2.2. *PL characteristics*

Fig. 16 (a) shows the PL spectra of the NCs with and without ligands (URSOA-WL and URSOA-WOL) where the PL peaks for both NCs are observed at almost the same wavelengths of 523 and 525 nm, respectively. The NCs with ligands (URSOA-WL) exhibit a stronger PL intensity than the NCs without ligands (URSOA-WOL). Based on the XPS results described above, defect species are not observed at the NC surface in the case of the NCs with ligands (URSOA-WL). Under these circumstances, the radiative recombination could be more predominant than the non-radiative recombination, leading to intense PL intensity. In contrast, in the case of the NCs without ligands (URSOA-WOL), the NCs could form the surface defect species which may form the trap states within the band gap.[89] The excitons trapped at the surface defect species could exhibit non-radiative recombination process. Thus, weaker PL intensity observed for the NCs without ligands (URSOA-WOL) may be caused by the surface defect species which might act as non-radiative decay center.

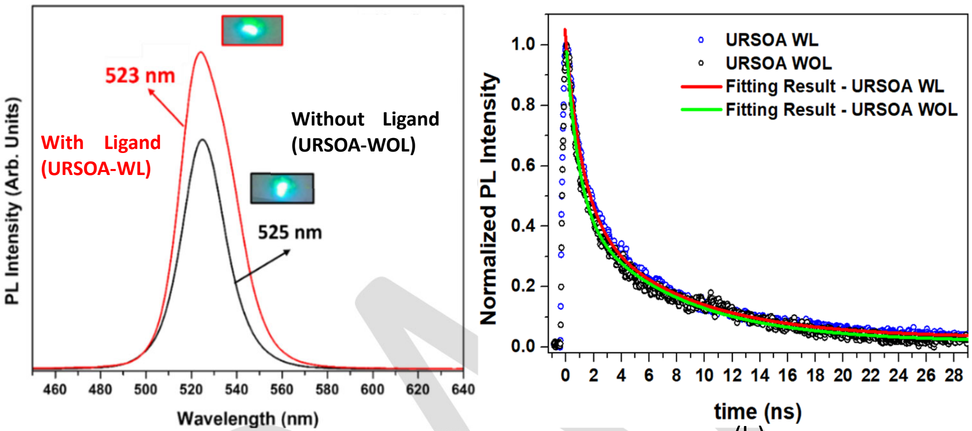

(a) (b)

Fig. 16. (a) PL spectra of the NCs prepared by URSOA method: the NCs with (red line) and without ligands (black line). (b) The normalized intensity of PL as a function of time measured for the URSOA-WL and URSOA-WOL NCs. The fitting results are also shown as solid lines.

The PL decays observed in the NCs prepared by the URSOA method (URSOA-WL and URSOA-WOL) show almost similar decay characteristics, as seen in Fig. 16 (b). These PL decays were fitted using a bi-exponential function with two distinct decay time constants, including their average decay time.[70,71] The PL decays in Fig. 16 (b) and the fitting results (Table 3) indicate that the NCs prepared by the URSOA method (URSOA-WL and URSOA-WOL) exhibit indistinguishable decay features. This fact implies that the excitons in these NCs might not be affected by the ligands and the surface defect species. According to the previous study, due to the zero-dimensional (0D) characteristics of Cs_4PbBr_6 crystal structure, strong exciton confinement might occur in the isolated individual $[PbBr_6]^{4-}$ octahedron.[17] Although the NCs prepared by the URSOA method contain Cs_4PbBr_6 and $CsPbBr_3$ phases with the ratio of nearly equals to 10:1, the PL might be predominantly occurred on the Cs_4PbBr_6 NCs. The contribution from $CsPbBr_3$ NCs in the PL spectra is not seen because the PL peak of $CsPbBr_3$ NCs is slightly red-shifted to a wavelength longer than 525 nm, as described in 4.1.2. The PL characteristics of these URSOA NCs indicate a higher exciton confinement in the Cs_4PbBr_6 NCs phase compared to the $CsPbBr_3$ NCs phase.[18,90] Regarding the possibility of phase ratio changes, it should be noted that such phase change can be disregarded by considering the XRD data of those URSOA NCs, which show the similar phase composition (hexagonal Cs_4PbBr_6 and orthorhombic CsPbBr3) in URSOA NCs with and without ligands (URSOA-WL and -WOL NCs). Therefore, a slight increase in the PL intensity of the URSOA-WL is originated from the surface ligands, which act as passivation molecules.

Table 3. The fitting results obtained from the curve fittings of PL decays in Fig. 16 (b) using a bi-exponential function. I_1 and I_2 are the normalized initial intensities.

Sample	I_1	**τ_1 (ns)**	I_2	**τ_2 (ns)**	**τ_{avg} (ns)**
NCs with Ligand (URSOA-WL)	0.55	1.22	0.43	7.26	6.19
NCs without Ligand (URSOA-WOL)	0.55	1.06	0.42	7.23	6.14

3.3. Comparison between NCs obtained from LARP and URSOA synthesis methods

First of all, we discuss the influence of synthesis methods on the crystal structures of the resulting NCs. Although both LARP and URSOA methods incorporate similar synthesis steps and precursor compositions, the resulting NCs have different crystal structures. The LARP method yielded orthorhombic $CsPbBr_3$ NCs. However, the URSOA method yielded a mixture of the orthorhombic $CsPbBr_3$ phase and the hexagonal Cs_4PbBr_6 NCs phase, where the phase molar ratio of Cs_4PbBr_6:$CsPbBr_3$ is nearly equal to 10:1. The LARP method facilitates a gradual crystallization process, resulting in the high crystal symmetry $CsPbBr_3$ NCs. In contrast, in the URSOA method, ultrasonic waves may lead to cavitation effects and localized heating, characterized by intense atomic vibrations. This condition may hinder the formation of highly symmetric crystal structures. Under these conditions, ultrasonication tends to produce Cs_4PbBr_6 NCs more preferentially rather than $CsPbBr_3$ NCs.[29]

Next, we discuss the relationship between the ligand and the surface chemical states. In the LARP method, LA could dissociate into a linoleate anion (L^-) and proton (H^+), in which the L^- anion tends to act as Lewis acids. During the crystal (surface) formation, the L^- anion might bond to the Cs^+ and Pb^{2+} cations by using carboxyl $-COO^-$ group whereas H^+ may bond to the Br atom (as shown in Fig. 8).[51,62,91] Therefore, the LA molecules might prevent the formation of defect states at the NC surface. In the absence of the LA ligand, since the Cs, Pb, and Br atoms at the NC surface might be unstable, these atoms could be easily removed from their sites in the crystalline structure, forming the accumulations of Cs^+, Pb^0, unbonded Br atoms, and Br vacancies at the NC surface. In the URSOA method, on the other hand, two kinds of ligands, namely LA and OlAm were used. The LA molecules might dissociate into L^- and H^+, where L^- could bond to the Cs^+ and Pb^{2+} cations and H^+ bond to Br^- anions at the NC surface. In addition, H^+ might interact with NH_2 species of the OlAm molecules, forming $OlAm^+$ or $–NH_3^+$ cations.[14,91] These cations could bond to Br^- anions at the NC surface.[92] Several previous studies have highlighted the significance of the interaction between Br^- and ligands, particularly the formation of Br–oleylammonium on the NC surface. [93,94] This interaction facilitates robust passivation, thereby preventing the formation of Br vacancies and under-coordinated Pb^{2+}.[93,94] Thus, the LA and the OlAm ligands could neutralize the surface defect species, including defect vacancies, and passivate the surface defect states that could act as non-radiative recombination centers. In contrast to NCs without those ligands, where the surface defect species, such as the accumulations of Cs^+, Pb^0, unbonded Br atoms, and Br vacancies, were formed at the NC surface, the presence of ligands evidently prevents the formation of those surface defect species.

Finally, we also need to discuss the difference in PL characteristics observed in the NCs prepared by the LARP and URSOA methods in relation to their surface chemical states The PL of LARP NCs mainly seems weaker than the URSOA NCs. In the LARP method, we did not use OlAm ligand during the synthesis. In the URSOA method, however, OlAm ligand was used in addition to OA ligand. It has been reported the formation of Br–oleylammonium provides strong passivation and can stabilize excitons on the NC surface, which thus results in high photoluminescence efficiency. [93–95] The presence of only Cs–oleate cannot provide effective passivation, resulting in a large number of trap states and reducing photoluminescence efficiency.[93] Therefore, these facts strongly emphasize the effect of ligands on PL characteristics by minimizing the non-radiative recombination sites on the surface of NCs.

In addition, it is also important to consider also the difference of PL characteristics in those LARP and URSOA in relation to their crystal structures. The PL characteristics of the LARP $CsPbBr_3$ NCs will be related to its orthorhombic crystal structure, where the $[PbBr_6]^{4-}$ octahedrons are continuously connected through a corner-sharing arrangement to form a 3D network[76], as illustrated in Fig. 10 (b). This 3D network facilitates the formation of excitons with large Bohr radius and long diffusion length.[96,97] Certain excitons may diffuse towards the surfaces of the NCs, where they subsequently emit PL. However, certain excitons may be trapped at the surface defect sites, which can undergo nonradiative recombination or emit PL at a lower photon energy and intensity. Consequently, PL quenching may occur and shorten the PL lifetime, as observed in the NCs without ligand (LARP-WOL). Different situation occurs in the URSOA NCs consisting of the predominant Cs_4PbBr_6 NCs structure, where each $[PbBr_6]^{4-}$ octahedron is surrounded by the Cs atoms being isolated without sharing the corner atoms with neighboring $[PbBr_6]^{4-}$ octahedron (Fig. 10 (c)). In this arrangement, $[PbBr_6]^{4-}$ octahedron could be rather isolated, forming 0D arrangement.[28,90] This 0D arrangement could confine the excitons within the individual octahedra, showing the excitons with a smaller Bohr radius.[90,98] As a result, the peak position does not change and PL intensity is just slightly decreased.

4. Conclusion

Cesium lead bromide perovskite NCs have been synthesized using the LARP and URSOA methods, where those methods used similar processing steps and precursor solutions. However, the crystal structures prepared by these methods were significantly different from each other. The LARP method yielded the $CsPbBr_3$ NCs with orthorhombic crystal structures, whereas the URSOA method yielded a mixture of hexagonal Cs_4PbBr_6 and orthorhombic $CsPbBr_3$ NCs. From HAXPES, it was found that the chemical states of the interior or inner side of the NCs were not affected by the presence or absence of the ligands. On the other hand, from XPS, the NCs without the ligand showed additional chemical states originating from the accumulation of Cs cations, Pb^0, unbonded Br atoms, and Br vacancies at the NCs surface. These surface chemical states can be then associated with surface defects, which can act as non-radiative recombination sites. The PL of the LARP NCs exhibits two distinct PL decay components attributed to free and trapped excitons within the orthorhombic $CsPbBr_3$ crystal structure. This structure, characterized by its 3D nature, may facilitate exciton diffusion or migration to the surface of the NCs. Therefore, excitons reaching the NCs without ligands may undergo non-radiative recombination, resulting in a weak PL with a short PL lifetime. Here, excitons in $CsPbBr_3$ NCs are sensitive to surface states or surface defects. In contrast, despite the PL characteristics of the URSOA NCs also show two PL decay components, also suggesting the formation of free excitons and trapped excitons in the Cs_4PbBr_6 NCs, the PL characteristics of the NCs with and without ligands are not so sensitive to the presence or absence of ligands. This characteristic may be attributed to the 0D characteristics of the Cs_4PbBr_6 crystal structures, where excitons are more localized in the $PbBr_6$ octahedron without long migration or diffusion to the NCs surface. Therefore, URSOA NCs are more tolerant of the presence of surface defects compared to LARP NCs. The present experimental findings in this study may provide new insight into the effect of ligands on the NCs surface structures, which is seen from the formation of additional surface chemical states originating from surface defect species, and their impact on PL characteristics of these lead halide perovskite materials. This insight may be useful not only for the further development of passivation molecules for halide perovskites in general but also for the design of buffer layer molecules in perovskite heterojunction devices.

Conflicts of interest

There are no conflicts of interest to declare.

Acknowledgements

This work was supported by Program Riset Internasional ITB of Bandung Institute of Technology 2022. This work was also partially supported by JSPS KAKENHI Grant number JP25K08480. MA gratefully acknowledge the NIMS Internship Program 2023-2024 of National Institute of Materials Science, Japan.

References

1 J. A. Sichert, Y. Tong, N. Mutz, M. Vollmer, S. Fischer, K. Z. Milowska, R. García Cortadella, B. Nickel, C. Cardenas-Daw, J. K. Stolarczyk, A. S. Urban and J. Feldmann, *Nano Lett.*, 2015, **15**, 6521–6527.
2 H. Wang, X. Li, M. Yuan and X. Yang, *Small*, 2018, **14**, 1703410.
3 C. Wehrenfennig, G. E. Eperon, M. B. Johnston, H. J. Snaith and L. M. Herz, *Adv. Mater.*, 2014, **26**, 1584–1589.
4 C. Bao, C. Chen, M. Muhammad, X. Ma, Z. Wang, Y. Liu, P. Chen, S. Chen, B. Liu, J. Wang and Y. Duan, *Org. Electron.*, 2019, **73**, 299–303.
5 H. Wang, J. Lei, F. Gao, Z. Yang, D. Yang, J. Jiang, J. Li, X. Hu, X. Ren, B. Liu, J. Liu, H. Lei, Z. Liu and S. (Frank) Liu, *ACS Appl. Mater. Interfaces*, 2017, **9**, 21756–21762.
6 L. Dou, Y. Yang, J. You, Z. Hong, W.-H. Chang, G. Li and Y. Yang, *Nat. Commun.*, 2014, **5**, 5404.
7 S. A. Veldhuis, P. P. Boix, N. Yantara, M. Li, T. C. Sum, N. Mathews and S. G. Mhaisalkar, *Adv. Mater.*, 2016, **28**, 6804–6834.
8 M. A. Triana, E.-L. Hsiang, C. Zhang, Y. Dong and S.-T. Wu, *ACS Energy Lett.*, 2022, **7**, 1001–1020.
9 Y. Zhou and Y. Zhao, *Energy Environ. Sci.*, 2019, **12**, 1495–1511.
10 B. S. Swain, Md. A. K. Sheikh, S. Singh, R. Abdur, D. Jeong and J. Lee, *Mater. Sci. Semicond. Process.*, 2018, **74**, 361–368.
11 B. Tang, Y. Hu, H. Dong, L. Sun, B. Zhao, X. Jiang and L. Zhang, *Angew. Chem. Int. Ed.*, 2019, **58**, 16134–16140.
12 J. Deng, J. Li, Z. Yang and M. Wang, *J. Mater. Chem. C*, 2019, **7**, 12415–12440.
13 Y. Zhang, G. Hou, Y. Wu, M. Chen, Y. Dai, S. Liu, Q. Zhao, H. Lin, J. Fang, C. Jing and J. Chu, *Langmuir*, 2023, **39**, 6222–6230.
14 F. Haydous, J. M. Gardner and U. B. Cappel, *J. Mater. Chem. A*, 2021, **9**, 23419–23443.
15 M. V. Kovalenko, L. Protesescu and M. I. Bodnarchuk, *Science*, 2017, **358**, 745–750.
16 S. A. Kulkarni, S. G. Mhaisalkar, N. Mathews and P. P. Boix, *Small Methods*, 2019, **3**, 1800231.
17 J. Jancik, A. Jancik Prochazkova, M. C. Scharber, A. Kovalenko, J. Másilko, N. S. Sariciftci, M. Weiter and J. Krajcovic, *Cryst. Growth Des.*, 2020, **20**, 1388–1393.
18 L. Rao, X. Ding, X. Du, G. Liang, Y. Tang, K. Tang and J. Z. Zhang, *Beilstein J. Nanotechnol.*, 2019, **10**, 666–676.
19 P. Fu, Q. Shan, Y. Shang, J. Song, H. Zeng, Z. Ning and J. Gong, *Sci. Bull.*, 2017, **62**, 369–380.
20 D. Yang, M. Cao, Q. Zhong, P. Li, X. Zhang and Q. Zhang, *J. Mater. Chem. C*, 2019, **7**, 757–789.
21 G. B. Nair, R. Krishnan, A. Janse Van Vuuren and H. C. Swart, *Dalton Trans.*, 2023, **52**, 70–80.
22 W. Yao, D. Li, H. Wang and L. Yang, *J. Mater. Sci. Mater. Electron.*, 2019, **30**, 180–188.
23 C. Xie, J. He, Y. Zhu, L. Chen and P. Yang, *J. Lumin.*, 2022, **252**, 119400.
24 J. Chen, J. Ren, Z. Li, H. Wang and Y. Hao, *Org. Electron.*, 2018, **56**, 59–67.
25 S. Bhaumik, S. A. Veldhuis, Y. F. Ng, M. Li, S. K. Muduli, T. C. Sum, B. Damodaran, S. Mhaisalkar and N. Mathews, *Chem. Commun.*, 2016, **52**, 7118–7121.
26 C. A. López, C. Abia, M. C. Alvarez-Galván, B.-K. Hong, M. V. Martínez-Huerta, F. Serrano-Sánchez, F. Carrascoso, A. Castellanos-Gómez, M. T. Fernández-Díaz and J. A. Alonso, *ACS Omega*, 2020, **5**, 5931–5938.
27 V. R. Yandri, A. A. Nurunnizar, R. Debora, P. Wulandari, N. M. Nursam, R. Hidayat, E. D. Indari and Y. Yamashita, *Heliyon*, 2024, **10**, e23276.

28 L. Rao, B. Sun, Q. Zhang, M. Wen, J. Zhang, G. Zhong, T. Fu, X. Niu and Y. Tang, *Opt. Express*, 2022, **30**, 45376.

29 X. Xu, H. He, Z. Fang, H. Lou, C. Lin, L. Chen and Z. Ye, *ACS Appl. Nano Mater.*, 2019, **2**, 6874–6879.

30 R. Akimoto, M. Kobayashi and T. Suzuki, *J. Phys. Condens. Matter*, 1996, **8**, 105–110.

31 D. Marongiu, M. Saba, F. Quochi, A. Mura and G. Bongiovanni, *J. Mater. Chem. C*, 2019, **7**, 12006–12018.

32 W. Tao, Y. Zhang and H. Zhu, *Acc. Chem. Res.*, 2022, **55**, 345–353.

33 Y. Pan, J. Wang, Z. Sun, J. Zhang, Z. Zhou, C. Shi, S. Liu, F. Ren, R. Chen, Y. Cai, H. Sun, B. Liu, Z. Zhang, Z. Zhao, Z. Cai, X. Qin, Z. Zhao, Y. Ji, N. Li, W. Huang, Z. Liu and W. Chen, *Nat. Commun.*, 2024, **15**, 7335.

34 W. Xu, Y. Gao, W. Ming, F. He, J. Li, X. Zhu, F. Kang, J. Li and G. Wei, *Adv. Mater.*, 2020, **32**, 2003965.

35 H. Cheng, Y. Feng, Y. Fu, Y. Zheng, Y. Shao and Y. Bai, *J. Mater. Chem. C*, 2022, **10**, 13590–13610.

36 M. L. Agiorgousis, Y.-Y. Sun, H. Zeng and S. Zhang, *J. Am. Chem. Soc.*, 2014, **136**, 14570–14575.

37 D. Xu, Q. Wan, S. Wu, Y. Zhao, X. Xu, L. Li and G. He, *RSC Adv.*, 2020, **10**, 17653–17659.

38 S. Akhil, V. G. V. Dutt and N. Mishra, *Nanoscale Adv.*, 2021, **3**, 2547–2553.

39 J. J. L. Humphrey, S. Sadasivan, D. Plana, V. Celorrio, R. A. Tooze and D. J. Fermín, *Chem. – Eur. J.*, 2015, **21**, 12694–12701.

40 M. Rodová, J. Brožek, K. Knížek and K. Nitsch, *J. Therm. Anal. Calorim.*, 2003, **71**, 667–673.

41 C. Tenailleau, S. Aharon, B.-E. Cohen and L. Etgar, *Nanoscale Adv.*, 2019, **1**, 147–153.

42 A. Hardiansyah, W. J. Budiman, N. Yudasari, Isnaeni, T. Kida and A. Wibowo, *ACS Omega*, 2021, **6**, 32166–32177.

43 Y. Bai, M. Hao, S. Ding, P. Chen and L. Wang, *Adv. Mater.*, 2022, **34**, 2105958.

44 X. Wang, J. He, J. Li, G. Lu, F. Dong, T. Majima and M. Zhu, *Appl. Catal. B Environ.*, 2020, **277**, 119230.

45 X. Wang, F. You, J. Huang, Y. Yao and F. Xu, *Crystals*, 2022, **12**, 479.

46 H. Wu, J. Pi, D. Zhou, Q. Wang, Z. Long and J. Qiu, *Ceram. Int.*, 2022, **48**, 3383–3389.

47 N. Varnakavi, J. L. Velpugonda, N. Lee, S. Nah and L. Y. Lin, *Adv. Funct. Mater.*, 2024, 2413320.

48 S. Oswald, in *Encyclopedia of Analytical Chemistry*, ed. R. A. Meyers, Wiley, 1st edn., 2013.

49 F. A. Stevie and C. L. Donley, *J. Vac. Sci. Technol. Vac. Surf. Films*, 2020, **38**, 063204.

50 D. Wilson and M. A. Langell, *Appl. Surf. Sci.*, 2014, **303**, 6–13.

51 H. Han, J. Lee, D. W. Park and S. E. Shim, *Macromol. Res.*, 2010, **18**, 435–441.

52 J. Čechal and T. Šikola, *Appl. Surf. Sci.*, 2017, **423**, 538–541.

53 D. J. Morgan, *Surf. Interface Anal.*, 2024, sia.7360.

54 D. R. Baer, K. Artyushkova, H. Cohen, C. D. Easton, M. Engelhard, T. R. Gengenbach, G. Greczynski, P. Mack, D. J. Morgan and A. Roberts, *J. Vac. Sci. Technol. A*, 2020, **38**, 031204.

55 X. Wu, X. Zhang, W. Yu, Y. Zhou, W. Wong, W. He, K. P. Loh, X.-F. Jiang and Q.-H. Xu, *J. Mater. Chem. A*, 2023, **11**, 4292–4301.

56 A. Ali, H. Cruguel, E. Giangrisostomi, R. Ovsyannikov, M. G. Silly, L. Dudy, U. B. Cappel, E. Lhuillier, N. Witkowski and F. O. L. Johansson, *J. Phys. Chem. Lett.*, 2024, **15**, 3721–3727.

57 K. Kim, D. Kang, S. Blumstengel, N. Z. Morales, E. J. W. List-Kratochvil, S. W. Cho, H. Lee, S. Park and Y. Yi, *Appl. Phys. Rev.*, 2023, **10**, 041411.

58 S. J. Heo, S. Yoon, S. H. Oh and H. J. Kim, *Nanoscale Res. Lett.*, 2013, **8**, 488.

59 B. M. Abdullah, N. Salih and J. Salimon, *J. Saudi Chem. Soc.*, 2014, **18**, 276–287.

60 I. O. Perez De Berti, M. V. Cagnoli, G. Pecchi, J. L. Alessandrini, S. J. Stewart, J. F. Bengoa and S. G. Marchetti, *Nanotechnology*, 2013, **24**, 175601.

61 W. A. P. J. Premaratne, W. M. G. I. Priyadarshana, S. H. P. Gunawardena and A. A. P. De Alwis, *J. Sci. Univ. Kelaniya*, 2014, **8**, 33–48.

62 A. Kirakosyan, N. D. Chinh, M. R. Sihn, M.-G. Jeon, J.-R. Jeong, D. Kim, J. H. Jang and J. Choi, *J. Phys. Chem. Lett.*, 2019, **10**, 4222–4228.

63 J. A. Peters, Z. Liu, R. Yu, K. M. McCall, Y. He, M. G. Kanatzidis and B. W. Wessels, *Phys. Rev. B*, 2019, **100**, 235305.

64 A. A, A. Yadav, P. Vishnoi and D. K. Sharma, *Nanoscale*, 2025, **17**, 5150–5160.
65 B. Liu, X. Jia, Y. Nie, Y. Zhu and H. Ye, *Appl. Surf. Sci.*, 2022, **584**, 152626.
66 W. Liu, G. Yuan, Y. Zhang, Q. Wang, S. Zhao, Z. Liu, T. Wei, J. Wang and J. Li, *J. Mater. Chem. C*, 2019, **7**, 10783–10788.
67 L. Wang, H. Liu, Y. Zhang and O. F. Mohammed, *ACS Energy Lett.*, 2020, **5**, 87–99.
68 O. E. Solis, J. Manuel Rivas, A. A. Duran-Ledezma, A. Gonzalez-Cisneros, M. García-Rocha and D. Esparza, *Mater. Lett.*, 2021, **289**, 129392.
69 L. Rao, B. Sun, Y. Liu, G. Zhong, M. Wen, J. Zhang, T. Fu, S. Wang, F. Wang and X. Niu, *Nanomaterials*, 2023, **13**, 355.
70 J. A. Peters, Z. Liu, M. C. De Siena, M. G. Kanatzidis and B. W. Wessels, *J. Lumin.*, 2022, **243**, 118661.
71 N. Bel Haj Mohamed, M. Haouari, Z. Zaaboub, M. Nafoutti, F. Hassen, H. Maaref and H. Ben Ouada, *J. Nanoparticle Res.*, 2014, **16**, 2242.
72 H. He, Q. Yu, H. Li, J. Li, J. Si, Y. Jin, N. Wang, J. Wang, J. He, X. Wang, Y. Zhang and Z. Ye, *Nat. Commun.*, 2016, **7**, 10896.
73 H. Fiedler, J. Hardy, J. E. Halpert, N. J. L. K. Davis and J. Kennedy, *Nanotechnology*, 2025, **36**, 065202.
74 M. Velázquez, A. Ferrier, S. Péchev, P. Gravereau, J.-P. Chaminade, X. Portier and R. Moncorgé, *J. Cryst. Growth*, 2008, **310**, 5458–5463.
75 M. Wang, Q. Yu, T. Yu, S. Zhang, M. Gong and Y. Liu, *RSC Adv.*, 2023, **13**, 5158–5167.
76 F. Palazon, C. Urso, L. De Trizio, Q. Akkerman, S. Marras, F. Locardi, I. Nelli, M. Ferretti, M. Prato and L. Manna, *ACS Energy Lett.*, 2017, **2**, 2445–2448.
77 C. K. Moller, *K. Dan. Vidensk. Selsk. Mat.-Fys. Meddelelser*, 1960, **32**, 1–13.
78 T. Monecke, S. Kohler, R. Kleeberg, P. M. Herzig and J. B. Gemmell, *Can. Mineral.*, 2001, **39**, 1617–1633.
79 T. W. Kang, Y. J. Park, G. J. Jeong, J. Hwang, J. H. Kim, J. S. Kim, B. Bae, K. Tota and S. W. Kim, *Inorg. Chem. Front.*, 2021, **8**, 2036–2041.
80 W. Sun, Y.-T. Hung, W.-T. Huang, R.-S. Liu and W. Zhou, *Cryst. Growth Des.*, 2024, **24**, 545–553.
81 Z. Shi, Y. Yang, X.-Y. Sun, F. Lang and L. Lin, *RSC Adv.*, 2021, **11**, 16453–16460.
82 Y. Li, W. Shao, L. Chen, J. Wang, J. Nie, H. Zhang, S. Zhang, R. Gao, X. Ouyang, X. Ouyang and Q. Xu, *NPG Asia Mater.*, 2021, **13**, 40.
83 X. Chen, F. Zhang, Y. Ge, L. Shi, S. Huang, J. Tang, Z. Lv, L. Zhang, B. Zou and H. Zhong, *Adv. Funct. Mater.*, 2018, **28**, 1706567.
84 D. Laishram, *Appl. Surf. Sci.*
85 I. A. Shuklov, V. F. Toknova, D. V. Demkin, G. I. Lapushkin, L. M. Nikolenko, A. A. Lizunova, S. B. Brichkin, V. N. Vasilets and V. F. Razumov, .
86 Z. Fereshteh, M. Salavati-Niasari, K. Saberyan, S. M. Hosseinpour-Mashkani and F. Tavakoli, *J. Clust. Sci.*, 2012, **23**, 577–583.
87 Q. Huang, W. Yin, B. Gao, Q. Zeng, D. Yao, H. Zhang, Y. Zhao, W. Zheng, J. Zhang, X. Yang, X. Zhang and A. L. Rogach, *Light Sci. Appl.*, 2024, **13**, 111.
88 M. Giancaspro, A. Panniello, N. Depalo, R. Comparelli, M. Striccoli, M. L. Curri and E. Fanizza, *Nanomaterials*, 2023, **14**, 81.
89 H. Jin, E. Debroye, M. Keshavarz, I. G. Scheblykin, M. B. J. Roeffaers, J. Hofkens and J. A. Steele, *Mater. Horiz.*, 2020, **7**, 397–410.
90 M. I. Saidaminov, J. Almutlaq, S. Sarmah, I. Dursun, A. A. Zhumekenov, R. Begum, J. Pan, N. Cho, O. F. Mohammed and O. M. Bakr, *ACS Energy Lett.*, 2016, **1**, 840–845.
91 A. Soosaimanickam, A. Saura, N. Farinós and R. Abargues, *Nanoenergy Adv.*, 2023, **3**, 376–400.
92 J. De Roo, M. Ibáñez, P. Geiregat, G. Nedelcu, W. Walravens, J. Maes, J. C. Martins, I. Van Driessche, M. V. Kovalenko and Z. Hens, *ACS Nano*, 2016, **10**, 2071–2081.
93 L. De Trizio, I. Infante and L. Manna, *Acc. Chem. Res.*, 2023, **56**, 1815–1825.
94 Y. Zhao, S. Wei, X. Cao, Y. Liu, H. Chen, Z. Lu, L. Zhong and Y. Qiu, *Nano Energy*, 2025, **142**, 111246.

95 J. H. Park, A. Lee, J. C. Yu, Y. S. Nam, Y. Choi, J. Park and M. H. Song, *ACS Appl. Mater. Interfaces*, 2019, **11**, 8428–8435.

96 K. Lê, N. Heshmati and S. Mathur, *Nano Converg.*, 2023, **10**, 47.

97 L. Protesescu, S. Yakunin, M. I. Bodnarchuk, F. Krieg, R. Caputo, C. H. Hendon, R. X. Yang, A. Walsh and M. V. Kovalenko, *Nano Lett.*, 2015, **15**, 3692–3696.

98 H. Kim, J. H. Park, K. Kim, D. Lee, M. H. Song and J. Park, *Adv. Sci.*, 2022, **9**, 2104660.